Enhanced epithelial fluorescence sensitivity using an oblique-angled fiber optic probe for epithelial cancer diagnosis: a modified Monte Carlo simulation study

NEMICHAND,[1] SHIVAM SHUKLA,[2] PANKAJ SINGH,[3] AND ASIMA PRADHAN[1,2,4,*]

[1]*Department of Physics, Indian Institute of Technology Kanpur, Kanpur 208016, India*
[2]*Center for Lasers and Photonics, Indian Institute of Technology Kanpur, Kanpur 208016, India*
[3]*Department of Physics, Allahabad Degree College, Prayagraj, U.P., India*
[4]*Siksha 'O' Anusandhan (Deemed to be University), Bhubaneswar 751030, India*
*asima@iitk.ac.in

This study aims to analyze spatially resolved fluorescence for probing various depths of the epithelial tissue using an optimized illumination and collection configuration. The enhanced epithelial sensitivity enables precise detection of alterations in the tissue's optical properties associated with disease progression. The elastic scattering and fluorescence of a cervical tissue-mimicking phantom were simulated using the Monte Carlo method, which was modified to incorporate oblique illumination, oblique collection, and the propagation of fluorescence photons. The results demonstrate that oblique illumination and collection in a parallel configuration (O-O-P) exhibit high epithelial sensitivity at both small and large source–detector separations. Additionally, spatially resolved fluorescence enables high-sensitivity probing of various depths within the epithelium layer. We modeled a fiber-optic probe employing an O-O-P configuration with 45° beveled fibers. It was observed that this multi-collection fiber-optic probe effectively differentiates cervical precancer grades by analyzing fluorescence intensity variations, which correspond to changes in tissue optical properties during disease progression.   © 2025 Optica Publishing Group. All rights, including for text and data mining (TDM), Artificial Intelligence (AI) training, and similar technologies, are reserved.

1. INTRODUCTION

Light propagation in biological tissues is theoretically modeled by the radiative transport equation (RTE), though solving RTE for complex systems like tissues is challenging [1–3]. Monte Carlo simulation is a computational method equivalent to the RTE for modeling light transport in turbid media, estimating spatially resolved reflectance, internal fluence, fluorescence, and light transmission [4–7]. These simulations are crucial for optimizing the design of fiber-optic probes for *in vivo* clinical applications and accurately characterizing photon propagation in multilayered tissue geometries [8,9].

Fiber-optic probes are extensively utilized for targeted light delivery and collection in diffuse reflectance and fluorescence spectroscopy, serving as essential tools in disease diagnosis and treatment [10–13]. In epithelial cancers such as oral and cervical cancers, the configuration of the fiber-optic probe is particularly crucial for accessing the appropriate tissue depth to obtain accurate diagnostic information [13–15]. Epithelial tissues consist of a thin epithelium (100–600 μm) overlying a thicker stroma, each with distinct optical properties [16,17]. In these cancers,

biochemical and morphological changes typically originate at the epithelium–stroma interface, gradually spreading through the epithelial layer and eventually invading the stromal layer as the disease progresses [16,18,19].

Light propagation in the epithelial tissue is predominantly forward-directed, meaning that normal incident light tends to penetrate beyond the thin epithelial layer and into the underlying stroma [20]. Consequently, fiber-optic probes with a normal light illumination configuration often result in a large fraction of photons diffusing into the stroma, leading to higher sensitivity to the stromal layer rather than the epithelial layer [21]. This limits the ability of the fiber-optic probes to effectively detect subtle changes within the epithelial layer, where early-stage abnormalities typically occur. To improve diagnostic accuracy for epithelial cancers, it is crucial to design fiber-optic probes that diffuse a maximum fraction of illumination light into the epithelial layer. Optimizing light diffusion within the epithelial layer enhances the probe's sensitivity to detect subtle biochemical changes that occur in the initial stages of epithelial cancer. In the context of diffuse reflectance spectroscopy (DRS),

epithelial sensitivity is influenced by several factors, including the illumination–collection fiber configuration, the diameter of the illumination and collection fibers, and the source-detector separation (SDS) [9,13,22]. The epithelial sensitivity for normal illumination and normal collection (N-N) fiber-optic probe configuration decreases monotonically with increasing SDS [22]. The incident photons that penetrate deeper undergo multiple scattering interactions with molecules, causing deviations from their original paths and leading to their collection at larger SDS. Thus, epithelial sensitivity decreases with SDS, diminishing the ability to detect early-stage epithelial alterations. Therefore, optimizing these parameters is crucial for improving the probe's efficiency in capturing diagnostically significant signals from the epithelium. Oblique illumination fiber-optic probes enhance photon diffusion in the epithelial layer compared to normal illumination [22–24]. The increase in epithelial sensitivity occurs because oblique illumination enhances the photon interaction path within the epithelial layer. However, this enhanced sensitivity is most effective near the source fiber, which imposes limitations on the allowable diameter of both the illumination and collection fibers. A smaller fiber diameter may reduce the intensity of the illumination and photon collection, thereby affecting the overall efficiency of the probe in detecting subtle changes in the epithelial layer.

In recent years, fluorescence spectroscopy has emerged as a powerful tool for diagnosing epithelial cancers with high sensitivity, utilizing fluorescence biomarkers such as NADH, FAD, collagen, and porphyrin [25–33]. The interaction of light with fluorescent molecules in tissues has been extensively analyzed using Monte Carlo simulations by various research groups for the *in vivo* applications of fiber-optic probes [34–38]. Monte Carlo simulations for fluorescence provide highly accurate solutions for modeling light–tissue interactions, though they are computationally intensive. To address this limitation, some researchers have implemented diffusion approximations to reduce computation time for spatially resolved fluorescence studies [39–42]. Swartling *et al.* have developed an accelerated Monte Carlo simulation specifically for fluorescence in the epithelial tissue, significantly enhancing computational efficiency [43].

Pfefer *et al.* demonstrated that oblique illumination–collection fiber probe geometries are highly effective at collecting superficial fluorescence photons from the epithelial layer [37]. Their studies also identified the optimal collection angles for capturing epithelial fluorescence from the superficial tissue layers. Furthermore, *in vitro* studies conducted by our group have demonstrated that oblique illumination and collection in a parallel configuration (O-O-P) fiber-optic probe is particularly effective for diagnosing cervical cancer, especially when combined with artificial neural network algorithms for data analysis [44]. These studies underscore the importance of analyzing oblique illumination–collection fiber-optic probe geometries to optimize the position of the illumination and collection fibers, ensuring more efficient collection of epithelial fluorescence. This approach could significantly enhance the accuracy and effectiveness of fluorescence-based diagnostics for epithelial cancers.

In this study, a modified fluorescence Monte Carlo simulation was employed to model light propagation, fluorescence emission, and photon distribution within the tissue. The light–tissue interaction was simulated using a cervical tissue-mimicking model consisting of an epithelium layer overlying a stroma layer. The optimal oblique angle for the fiber-optic probe configuration, aimed at enhancing fluorescence from the epithelium, was determined through an analysis of light absorption and fluorescence collection efficiency. Based on this analysis, an oblique illumination and oblique collection in a parallel configuration (O-O-P) with a 45° oblique angle was implemented to efficiently illuminate the tissue and collect fluorescence from the epithelium layer. This configuration was used to analyze spatially resolved fluorescence and assess epithelial sensitivity for efficient fluorescence collection from different depths within the epithelium. Furthermore, these results were applied to simulate a fiber-optic probe for cervical cancer diagnosis, demonstrating its ability to detect subtle changes in the optical properties of cervical tissue as the disease progresses.

The main contributions of this paper are as follows:

1. A modified Monte Carlo simulation-based fluorescence study demonstrating enhanced sensitivity to the epithelial layer, crucial for early-stage cancer diagnosis.
2. Optimization of a fiber-optic probe geometry capable of differentiating spatially resolved fluorescence signals originating from different tissue depths.
3. A 45° beveled fiber-optic probe design with strong potential for use in *ex vivo* studies within clinical or point-of-care settings.

2. MATERIALS AND METHODS

A. Tissue-Mimicking Phantom Model and Optical Properties

A two-layer cervical tissue-mimicking phantom model, as shown in Fig. 1(a), was used to simulate the propagation of both elastically scattered and fluorescence photons. The top layer, with a thickness of 300 μm, represents the epithelium, while the bottom layer, the stroma, is modeled as a semi-infinite medium. All layers of the tissue-mimicking phantom were assumed to be homogeneous [33,45,46]. The optical properties of the medium at the excitation and fluorescence emission wavelengths were chosen to be the same [47,48]. These optical properties were kept similar to those of cervical tissue, as reported in the literature [49]. Incident photons are absorbed by both chromophores (molecules that do not emit photons) and fluorophores (molecules that emit photons at wavelengths longer than excitation). Since propagation of light in the epithelial tissue is predominantly forward-directed, the anisotropy factor for the top (epithelium) and bottom (stroma) layers was set at 0.95 and 0.80, respectively. Both layers were assigned a refractive index of 1.4. The quantum yield for the epithelium and stroma layers was assumed to be the same [13,39]. The oblique illumination–collection configuration was obtained using the bevel fibers with a core refractive index of 1.5, serving as the medium just above the tissue surface [Fig. 1(b)]. The half-acceptance angle was approximately 9°, corresponding to a numerical aperture (NA) of 0.22. The cervical epithelial layer, critical for histopathological analysis, is modeled with a total thickness of 300 μm and divided into three equal layers
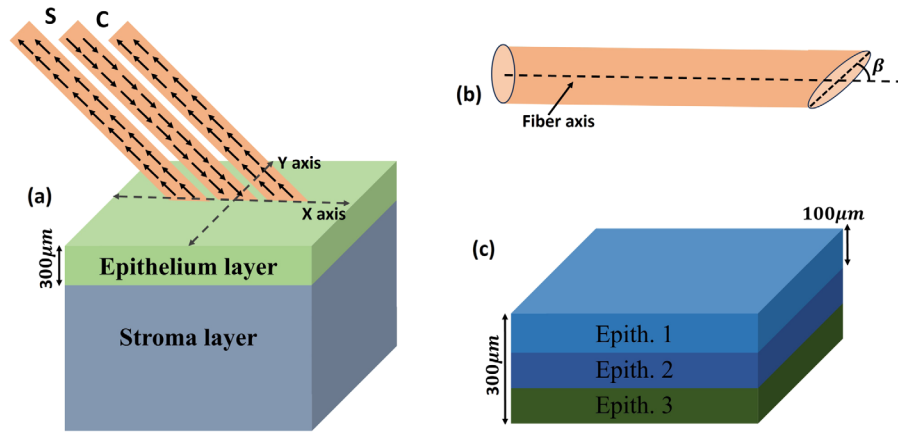
Fig. 1. (a) Oblique illumination and collection in a parallel configuration (O-O-P) on a tissue-mimicking phantom model consisting of a 300 μm epithelium layer and a semi-infinite stroma layer (S, source fiber; C, collection fiber). (b) A fiber with a bevel angle β. (c) The epithelium layer subdivided into three 100 μm thick sublayers (Epith1, Epith2, and Epith3), and each layer is assumed to be homogeneous and parallel to one another.

Table 1. Optical Properties for Different CIN Stages

		Normal		CIN 1		CIN 2		CIN 3			
Layer	n	μ_a	μ_s	μ_a	μ_s	μ_a	μ_s	μ_a	μ_s	g	d (cm)
Epith. 1	1.4	2.0	50	2.0	50	2.0	50	3.0	70	0.95	0.01
Epith. 2	1.4	2.0	50	2.0	50	3.0	70	3.0	70	0.95	0.01
Epith. 3	1.4	2.0	50	3.0	70	3.0	70	3.0	70	0.95	0.01
Stroma	1.4	4.0	250	4.0	250	4.0	250	4.0	250	0.80	10

of 100 μm each. This layered structure aligns with the clinical grading of cervical intraepithelial neoplasia (CIN), where the extent of abnormal cell growth within each third of the epithelium determines the CIN grade [50]. The optical parameters for the layers of the tissue-mimicking phantom model are provided in Table 1.

B. Modified Fluorescence Monte Carlo Simulation

The MCML program, written in C, simulates the propagation of light in a multilayered medium [1]. The original MCML program is limited to normal illumination and stores physical quantities in cylindrical grids. Due to the introduction of oblique illumination and collection geometry in our study, this cylindrical symmetry was broken. To address this, the necessary modifications were made to enable the storage of physical quantities on two-dimensional square grids and three-dimensional cubic grids.

Two distinct subroutines named excitation and emission, as shown in the flowchart (Fig. 2), were used to simulate the propagation of light for elastic scattering and fluorescence in the tissue-mimicking layered medium. The excitation subroutine simulates the incidence, propagation, and absorption of elastically scattered photons at the illumination wavelength. The initial position and direction of the incident photons are determined based on the bevel angle, diameter, and numerical aperture of the fiber. Photon propagation, scattering, absorption, and termination are governed by the Monte Carlo rules for a multilayer medium [1]. We have used 10^8 number of photons, which consumes approximately 3 h of simulation time. Each photon is initialized with a weight of 1. The step size for photon

propagation is randomly sampled based on the probability density function derived from the optical properties of the medium. After propagating a step size, the photon undergoes an elastic scattering interaction and changes its direction, which is sampled using the Henyey–Greenstein phase function [51]. At the end of each step, the photon's weight is reduced according to the absorption probability, and the absorbed fraction is recorded in a three-dimensional cubic grid with a spatial resolution of 0.001 cm. The absorption by fluorophores $[A_f(x, y, z)]$ and chromophores $[A_a(x, y, z)]$ is calculated from the accumulated weights. The spatially resolved quantities from photons exiting the surface of the medium are calculated as epithelial diffuse reflectance $R_d^e(x, y)$, total diffuse reflectance $R_d(x, y)$, and epithelial sensitivity $EpS_r(x, y)$ using Eqs. (1)–(3), where z denotes the maximum propagation depth:

$$R_d^e(x, y) = \sum_{z=0}^{z_e} R_d(x, y, z), \tag{1}$$

$$R_d(x, y) = \sum_{z=0}^{z_t} R_d(x, y, z), \tag{2}$$

$$EpS_r(x, y) = \frac{R_d^e(x, y)}{R_d(x, y)}. \tag{3}$$

In the emission subroutine, fluorescence photons are generated from the centers of the cubic grid, where photon absorption by fluorophores was recorded during the excitation subroutine. Each grid emits 2×10^3 fluorescence photons [52], which propagate through the medium according to the Monte Carlo rule, using the optical properties at the emission wavelength. The weights of fluorescence photons exiting the tissue surface, denoted as $S(N_{x1}, N_{y1}, N_z)$, are stored in cubic grids with a spatial resolution of 0.001 cm. These weights are then multiplied by the corresponding absorbed excitation weights to calculate the emitted fluorescence. The resulting fluorescence distribution is recorded in a 3D matrix, where x and y represent the spatial position of photon collection, and the z-coordinate indicates the depth at which the fluorescence photon originates. The
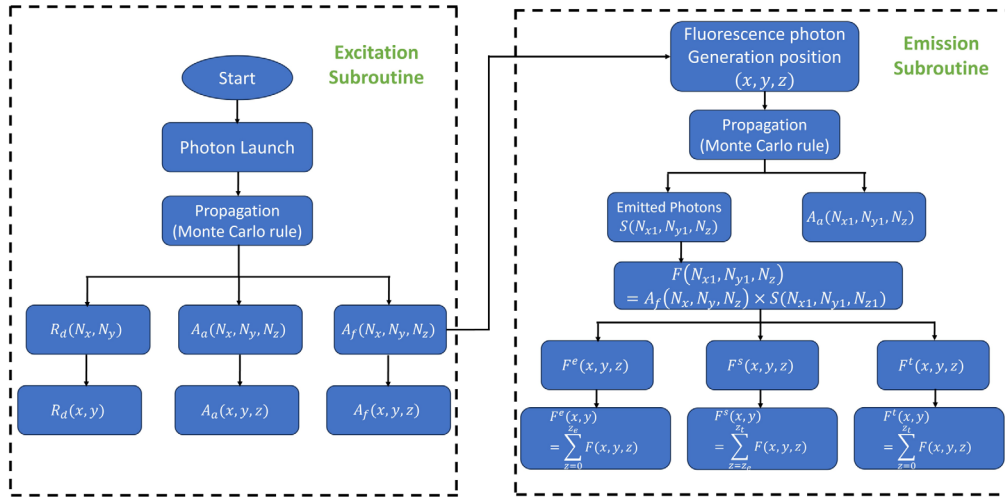
Fig. 2.   Flowchart of the modified fluorescence Monte Carlo Simulation.
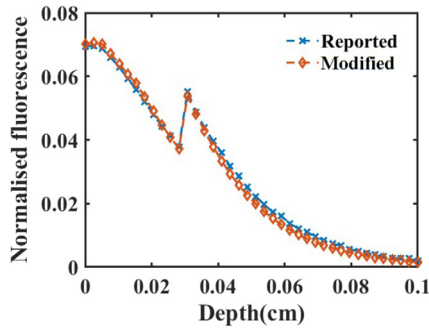

Fig. 3.   Validation of the modified fluorescence Monte Carlo simulation with depth-resolved fluorescence data reported in the literature (RMSE: 0.0016; p-value: 0.9990), based on the tissue-mimicking optical properties of aorta tissue ($n_{tissue} = 1.4$, $n_{fiber} = 1.5$, and $NA = 0.22$).

spatially resolved quantities—epithelial fluorescence $F^e(x, y)$, total fluorescence $F^t(x, y)$, and epithelial sensitivity EpS_f are calculated using Eqs. (4)–(6), where z denotes the position of the fluorescence photon origin:

$$F^e(x, y) = \sum_{z=0}^{z_e} F(x, y, z), \tag{4}$$

$$F^t(x, y) = \sum_{z=0}^{z_t} F(x, y, z), \tag{5}$$

$$EpS_f(x, y) = \frac{F^e(x, y)}{F^t(x, y)}. \tag{6}$$

The emission subroutine is computationally extensive and requires approximately 9–10 h of simulation. The results from the modified code have been validated against the fluorescence simulation results reported in the literature [51] and found good agreement (Fig. 3 shows one of the results).

3. RESULTS AND DISCUSSION

To investigate light–tissue interaction in epithelial tissues, a tissue-mimicking model was developed and simulated using a modified fluorescence Monte Carlo approach. This simulation aimed to optimize both light illumination and fluorescence collection for effective probing of epithelial layers. First, we examined the optimal oblique angle for a fiber-optic probe in oblique illumination and collection in a parallel configuration (O-O-P) to enhance sensitivity to epithelial fluorescence. Next, spatially resolved fluorescence was analyzed to identify the optimal positions for selectively probing different sublayers within the tissue. Further, a simple fiber-optic probe was designed and tested for its potential in fluorescence-based diagnosis of epithelial cancer.

A. Optimization of Light Illumination and Collection Angle

The tissue-mimicking model for optical properties of normal (given in Table 1) was simulated for light incidence at an oblique angle of 0° (normal incidence), 15°, 30°, 45°, and 60°. The cross-sectional view of the light absorption in the plane of incidence can be seen in Fig. 4. For oblique illumination, photons were launched with initial direction cosines determined by the fiber's numerical aperture, diameter, and the refractive indices of the fiber and the surrounding medium. Due to the fiber being beveled along the x-axis, the photons are launched asymmetrically along the x-axis and symmetrically along the y-axis. This directional asymmetry alters light absorption along the plane of incidence. The epithelium layer has lower scattering and a higher anisotropy factor than the stroma layer, so light mainly propagates in the incident direction in the epithelium layer. In the stroma layer, due to a higher scattering coefficient and a low anisotropy factor, photons get scattered isotropically. Compared to normal incidence, oblique illumination increases the effective photon path length within the epithelium, leading to enhanced scattering and improved superficial tissue sampling. At normal incidence ($\phi = 0°$), absorption is symmetric and centered around the illumination point, as shown in Fig. 4(b).
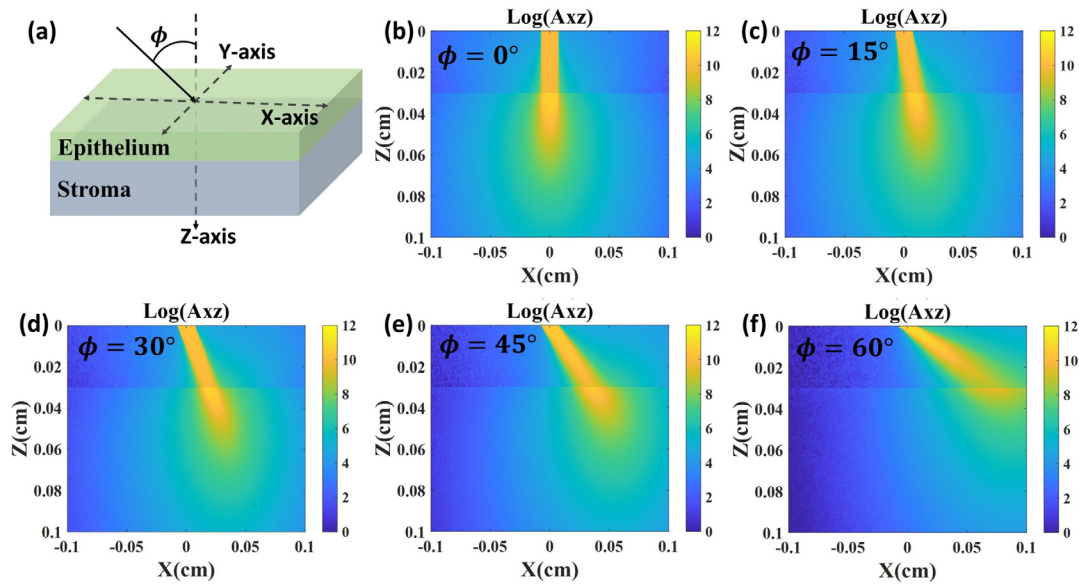
Fig. 4. (a) Tissue-mimicking model for simulation of light absorption with light incidence at an oblique angle ϕ from the normal. Light absorption along the plane of light incidence for oblique angles (ϕ): (b) 0° (normal incidence), (c) 15°, (d) 30°, (e) 45°, and (f) 60°.
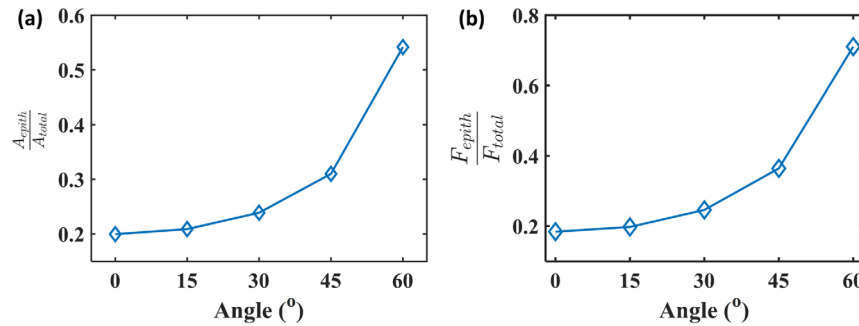

Fig. 5. (a) Fractional epithelial absorption and (b) fractional epithelial fluorescence for varying oblique angles (ϕ): 0° (normal incidence), 15°, 30°, 45°, and 60° for light illumination and collection.

As the angle increases, the absorption profile shifts laterally and becomes more asymmetric, with higher absorption occurring farther from the point of incidence [Figs. 4(c)–4(f)]. This indicates that oblique illumination enables light to propagate laterally within the epithelium, enhancing fluorescence excitation and detection from regions distant from the illumination position. It is also noted that the depth penetration within the tissue decreases with increasing light incidence angle. To find out the amount of photon absorption in the epithelium (A_{epith}) relative to the total absorption (A_{total}), we have calculated the fractional epithelial absorption $A_f^e = A_{epith}/A_{total}$, as shown in Fig. 5(a). The values of the fractional epithelial absorption for incidence angles of 0° (normal incidence), 15°, 30°, 45°, and 60° are 19.9%, 20.9%, 23.8%, 31.0%, and 54.2%, respectively. The fluorescence photon generation within the tissue is directly proportional to photon absorption; higher absorption in the epithelium layer results in enhanced fluorescence photon emission. We have calculated the fluorescence emitted from the epithelium and stroma separately using the emission subroutine of our modified Monte Carlo simulation. A quantity called fractional epithelial fluorescence was estimated as $F_f^e = F_{epith}/F_{total}$, where F_{epith} and F_{total} are epithelium fluorescence and total

fluorescence, respectively. The fractional epithelial fluorescence values for oblique angles of 0° (normal incidence), 15°, 30°, 45°, and 60° are found to be 18.4%, 19.8%, 24.6%, 36.4%, and 71.0%, respectively. Figures 5(a) and 5(b) collectively demonstrate that both epithelial absorption and fluorescence collection increase with an oblique angle, suggesting that higher oblique angles in the O-O-P configuration enhance the efficiency of epithelial fluorescence collection.

The optimal angle selected for our study is 45°, as it ensures reliable and efficient light transmission from the fiber to the medium without approaching the critical angle for total internal reflection (TIR). When light is incident from a fiber with a refractive index of $n = 1.5$ onto a medium with $n = 1.4$ (Table 1) at a 60° oblique angle, it forms a cone with a half acceptance angle of approximately 9°, with incident angles ranging from 51° to 69°. The critical angle for TIR at this interface is approximately 68.9°. As the incident angles approach this critical value, the risk of reflection losses increases, leading to reduced transmission efficiency [23,53]. To avoid these issues and ensure more efficient light illumination, an O-O-P configuration with a 45° oblique angle was selected for further analysis.
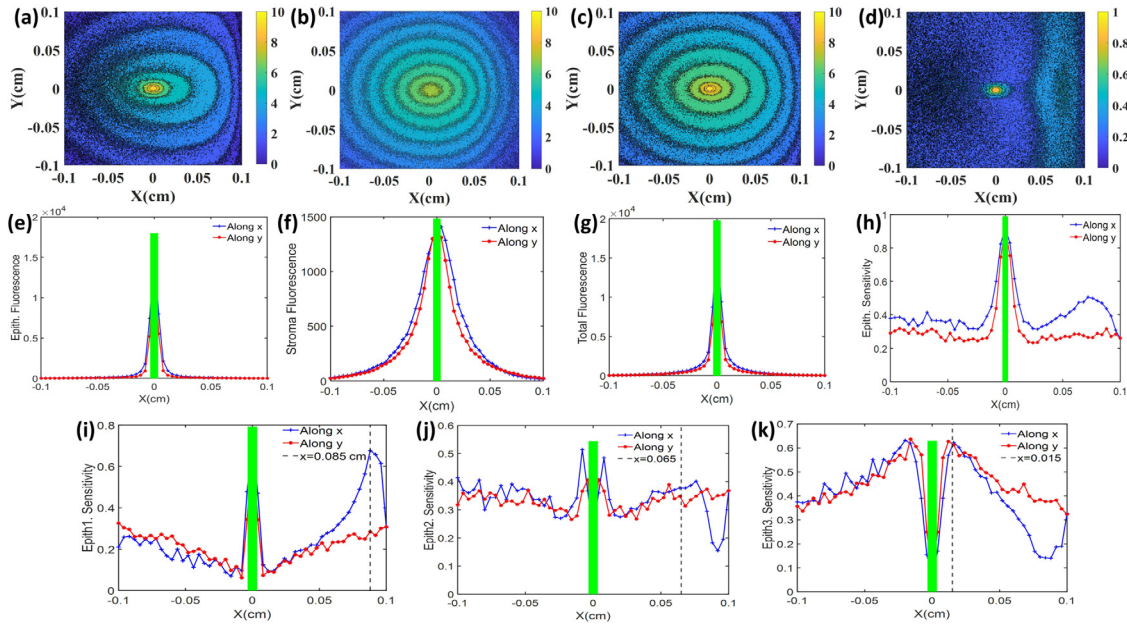
Fig. 6. Spatially resolved fluorescence and layer sensitivity analysis for the O-O-P configuration with a 45° oblique angle: (a–d) spatial maps of epithelium fluorescence, stroma fluorescence, total fluorescence, and epithelial sensitivity, respectively; (e)–(h) Corresponding line plots along the x- and y-axes; (i)–(k) layered fluorescence sensitivity for the epithelium sublayers Epith1, Epith2, and Epith3.

B. Spatially Resolved Fluorescence

Monte Carlo simulation was performed for spatially resolved fluorescence for a tissue-mimicking phantom using a modified fluorescence Monte Carlo program, as described in Section 2.B. A fiber of diameter 50 μm, oriented along the X axis, as shown in Fig. 4(a), was used for light illumination at a 45° oblique angle. Fluorescence collection was simulated using a 45° oblique configuration parallel to the illumination fiber. A normal tissue having optical properties mentioned in Table 1 has been utilized for our simulation. Fluorescence from the epithelium and stroma layers was analyzed separately to assess the individual contributions. A quantity called spatially resolved fluorescence sensitivity $E_p S_f$ was calculated using the individual contribution, as shown in Eq. (6). Simulated spatially resolved epithelium, stroma, total fluorescence, and epithelial sensitivity can be visualized in Figs. 6(a)–6(d). The epithelium, stroma, and total fluorescence are found almost symmetric about the point of illumination, which can be seen in Figs. 6(e)–6(g). However, the epithelial sensitivity is found to be asymmetric, as shown in Fig. 6(h). The linear epithelial sensitivity plot reveals enhanced sensitivity along the x-axis compared to the y-axis for all source–detector separations [Fig. 6(h)]. Along the y-axis, the sensitivity decreases monotonically, while along the x-axis, it initially decreases from the source position to 0.03 cm, then increases to a maximum value at approximately 0.0760 cm. The fluorescence intensity is highest at the center of the illumination fiber, which is the point of light incidence. These linear plots indicate that the high fluorescence intensity at the source location masks the subtle variations in intensity observed at larger source–detector separations. Further, it is important to probe the various layers of the epithelium to efficiently diagnose cervical cancer. Thus, the whole epithelium layer of 300 μm is subdivided into three layers of 100 μm each, as shown

in Fig. 1(c). To analyze the contribution of individual layer fluorescence in the epithelium fluorescence, a quantity called spatially resolved layered sensitivity ($E_p S_l$) is calculated as the fraction of fluorescence collected from a specific layer relative to the total fluorescence collected from the epithelium layer, as shown in Eq. (7). The linear plots of the layered sensitivity for the Epith1, Epith2, and Epith3 layers along the direction of light incidence and its normal are shown in Figs. 6(i)–6(k). The sensitivity of the Epith1 layer increases to a maximum of 0.68 at a position $x_1 = +0.085$ cm from the source. The changes in the optical properties of this layer can be efficiently captured by positioning the collection fiber at x_1. The sensitivity of Epith2 is maximum at $x = +0.008$ cm, which is close to the source fiber, and higher values are observed in the region from $x = +0.06$ cm to $x = +0.07$ cm. Fluorescence collection at the position of maximum sensitivity is constrained by the diameters of the source and collection fibers. Therefore, fluorescence from this layer can be efficiently collected by positioning the fiber at $x_2 = 0.065$ cm. Fluorescence from the Epith3 layer, situated just above the stroma layer, can be efficiently collected by positioning the collection fiber at $x_3 = 0.016$ cm, which corresponds to the maximum sensitivity of the layer. Therefore, to efficiently probe the various sublayers of the epithelium using spatially resolved fluorescence, the collection fiber should be positioned at x_1, x_2, and x_3:

$$Ep \, S_l(x, y) = \frac{F^l(x, y)}{F^e(x, y)}. \qquad (7)$$

This analysis demonstrates that positioning the collection fiber at an optimal spatial position allows for efficient fluorescence collection from the desired depths within the tissue, which may be helpful for the diagnosis of epithelial cancer. Furthermore, a simple fiber-optic probe can be designed based
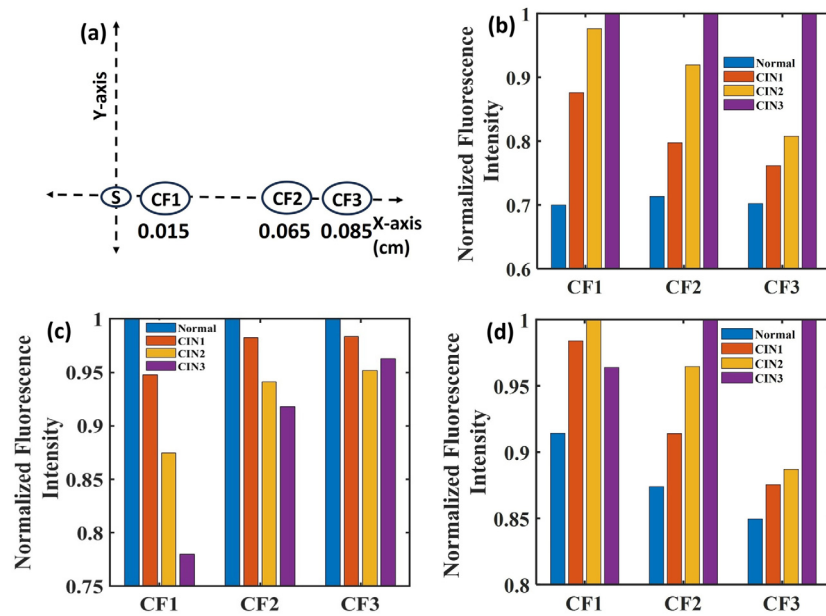
Fig. 7. (a) Schematic of the fiber-optic probe geometry used for epithelial fluorescence collection. (b) Normalized epithelial fluorescence, (c) normalized stromal fluorescence, and (d) total fluorescence for normal, CIN 1, CIN 2, and CIN 3 across collection fibers CF1, CF2, and CF3.

on the analysis done in this section to differentiate various cervical grades through fluorescence measurements.

C. Fiber-optic Probe for Diagnosis of Epithelial Cancer

In epithelial cancer, the morphological and biochemical characteristics of the tissue change with increasing abnormality, typically originating in the basal layer of the epithelium. These changes are classified as CIN 1 when they spread through up to one-third of the epithelium thickness, CIN 2 when they extend to two-thirds, and CIN 3 when the entire epithelium is affected [54,55]. The abnormality in the tissue changes the optical properties, which leads to changes in the intrinsic fluorescence of the tissue [21]. Therefore, it is crucial to simulate the fiber-optic probe to efficiently capture the variation in the tissue fluorescence, which may be helpful in the diagnosis of epithelial cancer.

The Monte Carlo fluorescence simulation conducted in this study suggests that 45° bevel fibers in a parallel configuration for light illumination and fluorescence collection, with multiple collection fibers positioned along the +X axis from the source fiber can be utilized to probe the alteration in optical properties of the epithelial tissue with disease progression. The tissue-mimicking phantom model used in the fluorescence Monte Carlo simulation is designed to replicate the characteristics of cervical precancer grading. We considered precancerous stages (CIN 1, CIN 2, and CIN 3) along with the normal tissue stage, with different optical properties for each grade (Table 1).

We have modeled an O-O-P fiber-optic probe consisting of a source fiber of 50 μm diameter positioned at the origin of the coordinate system and three collection fibers of diameter 100 μm, CF1, CF2, and CF3, positioned at $x = +0.015$ cm, $x = +0.065$ cm, and $x = +0.085$ cm respectively, along the +X axis, as shown in Fig. 7(a). These positions are selected on

the basis of the analysis of the previous section to efficiently capture the epithelial fluorescence originating from various layers of the epithelium.

Now, the fiber-optic probe consisting of three fibers, CF1, CF2, and CF3, is used to collect the epithelium, stroma, and total fluorescence from the epithelial tissue of different grades of precancer. To facilitate statistical comparison, the fluorescence intensity collected by each fiber was normalized relative to the maximum intensity. The epithelium, stroma, and total fluorescence intensities collected by the fiber-optic probe are shown sequentially in Fig. 7. As the disease progresses from the normal to the cancerous stage, light penetration decreases due to an increase in the optical properties, leading to an increase in epithelium fluorescence and a decrease in stromal fluorescence. The simulation results in Figs. 7(b) and 7(c) are found in the same pattern. The differences in fluorescence intensity shown in Figs. 7(b)–7(d) can further be used to differentiate among the various grades of cancer. The percentage fractional difference in fluorescence between two grades for each collection fiber is calculated using Eq. (8), where F_i and F_j represent the fluorescence intensities of the respective grades. Each element M_{ij} of the resulting matrix denotes the percentage fractional change in fluorescence intensity. Here, i and j correspond to the disease categories: normal, CIN 1, CIN 2, and CIN 3:

$$M_{ij} = \frac{|F_j - F_i|}{F_i} \times 100. \tag{8}$$

Figure 8 presents the matrix representation of the percentage fractional difference for the epithelium, stroma, and total fluorescence across all collection fibers and disease grades. The percentage variations in normalized fluorescence between consecutive grades are detailed in Table 2.

Figures 8(a)–8(c) present the matrix representation of the percentage fractional difference in epithelium fluorescence
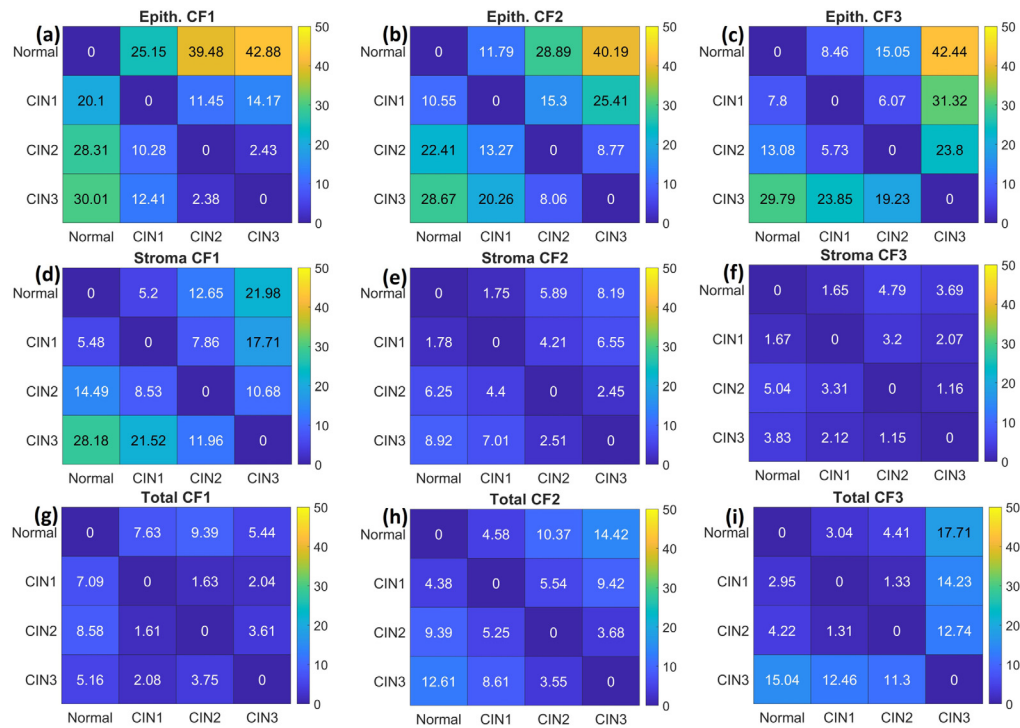
Fig. 8. Matrix representation of the fractional difference of fluorescence between two grades of cervical cancer. (a)–(c) correspond to epithelium fluorescence, (d)–(f) represent stroma fluorescence, and (g)–(i) depict total fluorescence for different collection fibers (CF1, CF2, and CF3).

Table 2.   Percentage Variation in Normalized Fluorescence Intensity for Different Collection Fibers

Fiber No.	$\frac{|CIN\,1 - Normal|}{Normal} \times 100$			$\frac{|CIN\,2 - CIN\,1|}{CIN\,1} \times 100$			$\frac{|CIN\,3 - CIN\,2|}{CIN\,2} \times 100$		
	Epith.	Stroma	Total	Epith.	Stroma	Total	Epith.	Stroma	Total
CF1	25.15	5.20	7.63	11.45	7.86	1.63	2.43	10.68	3.61
CF2	11.79	1.75	4.58	15.30	4.21	5.54	8.77	2.45	3.68
CF3	8.46	1.65	3.04	6.07	3.20	1.33	23.8	1.16	12.74

for collection fibers CF1, CF2, and CF3, respectively. The fractional differences between consecutive grades are listed in Table 2. The table indicates that the fractional difference in epithelium fluorescence between normal and CIN 1 grades is most pronounced with collection fiber CF1, which exhibits the highest percentage difference. This corresponds to changes primarily occurring in the Epith3 layer, as the sensitivity in Fig. 6(k) confirms high sensitivity near the CF1 position. For the CIN 1–CIN 2 transition, where variations in optical properties are predominantly found in the Epith2 layer, collection fiber CF2 shows the greatest percentage difference, aligning with the high sensitivity region for Epith2. Similarly, for distinguishing between CIN 2 and CIN 3, CF3 exhibits the highest difference, consistent with its sensitivity to the Epith1 layer. Figures 8(d)–8(f) present the matrix representation of the percentage fractional difference in stromal fluorescence for collection fibers CF1, CF2, and CF3, respectively. Table 2 shows that the CF1 fiber exhibits the maximum stroma fluorescence difference across all consecutive grades of the cervical tissue model.

Total fluorescence is a measurable quantity in fluorescence-based measurement in fiber-optic diagnostic devices. Figures 8(g)–8(i) present the percentage difference across all grades for each collection fiber. The fractional changes in fluorescence for transitions from normal to precancerous grades (CIN 1, CIN 2, and CIN 3) increase consistently with disease severity across all collection fibers. This trend is attributed to the progressive alteration in optical properties as the disease advances. This indicates that transitions from normal to higher-grade lesions can be distinguished with greater accuracy compared to transitions between lower-grade lesions. Table 2 shows that the maximum fractional differences for the transitions normal–CIN 1, CIN 1–CIN 2, and CIN 2–CIN 3 occur at collection fibers CF1, CF2, and CF3, respectively. These differences correspond to changes in the optical properties within the Epith3, Epith2, and Epith1 layers, which align with the high-sensitivity regions of collection fibers CF1, CF2, and CF3, respectively. Thus, the position of the collection fiber can differentiate between consecutive grades of cervical cancer using the spatially resolved fluorescence measurements.

The proposed fiber-optic probe enables clear differentiation between normal, CIN 1, CIN 2, and CIN 3 categories based on total fluorescence. The enhanced sensitivity at larger source–detector separations (SDS) plays a crucial role in distinguishing different cervical cancer grades, as demonstrated by the simulation results. This study highlights the necessity of positioning

the source and collection fibers in a manner that allows efficient probing of various epithelial tissue depths, as implemented here, to achieve higher diagnostic accuracy. Despite the relatively small variations in absorption and scattering coefficients considered in this study, the simulated illumination and fiber collection positions show a strong correlation with the observed results, thereby validating the effectiveness of the proposed fiber-optic probe design.

The proposed fiber-optic probe design demonstrates promising performance; however, several simplifications were necessary in the simulation to simplify the computational model, as described in Section 2.A. The assumption of identical optical properties at the excitation and emission wavelengths does not fully capture wavelength-dependent variation in light–tissue absorption and scattering. Epithelial tissues are not completely homogenous, as was assumed in the simulation; they are structurally and biochemically heterogeneous, with spatial variations in both optical properties and fluorophore distribution. The quantum yield of tissue layers depends on the biochemical composition of their constituent components. Accurately incorporating these would require greater computational resources and efforts. This simulated fiber-optics probe is a simple and implementable configuration, with fiber diameter and source–detector separation (SDS) values that are practically feasible and suitable for fabrication using standard fiber-optic components. The selected 45° oblique fiber arrangement in the O-O-P configuration is compatible with clinical applications, and the bevel-tip geometry can be fabricated using well-established polishing techniques. This design offers a promising foundation for future experimental validation and *in vivo* translation.

4. CONCLUSION

This study highlights the potential of fluorescence spectroscopy, combined with optimized fiber-optic probe design, for diagnosing epithelial precancer. A modified fluorescence Monte Carlo simulation was employed to model elastically scattered reflectance and fluorescence under oblique illumination and collection, incorporating both spatial and depth-resolved fluorescence. We evaluated the performance of an oblique-illumination and oblique-collection parallel (O-O-P) fiber-optic probe with a 45° beveled geometry. Simulation results demonstrated that this configuration effectively collects fluorescence signals from different epithelium depths, particularly near the illumination fiber and at larger source–detector separations (SDS). The findings show that fluorescence collection efficiency depends on the spatial positioning of the collection fibers, which must align with the depth of the targeted tissue layer. To address this, a probe with three collection fibers at varying SDS was designed to capture depth-specific fluorescence signals. The proposed fiber-optic probe effectively differentiates between normal–CIN 1, CIN 1–CIN 2, and CIN 2–CIN 3, with fractional total fluorescence intensity changes of 7.63%, 5.54%, and 12.74% observed at collection fibers CF1, CF2, and CF3, respectively. It enabled clear differentiation among mormal, CIN 1, CIN 2, and CIN 3 grades, demonstrating high sensitivity through fluorescence collection at optimized positions. Simulation results confirm that proper

spatial positioning of the source and collection fibers is essential for efficient depth-resolved probing and enhanced diagnostic accuracy in cervical precancer detection. Even with modest variations in optical properties, the observed trends align well with expectations, further validating the effectiveness of the probe design. In summary, this study offers valuable insights into optimizing fiber-optic probe geometry for depth-resolved tissue probing using spatially resolved fluorescence, enabling effective diagnosis of epithelial precancer. Future work will involve applying the proposed design in *in vivo* clinical studies to enhance cervical cancer detection.

REFERENCES

1. L. Wang, S. L. Jacques, and L. Zheng, "MCML—Monte Carlo modeling of light transport in multi-layered tissues," Comput. Methods Programs Biomed. **47**, 131–146 (1995).

2. C. Zhu and Q. Liu, "Review of Monte Carlo modeling of light transport in tissues," J. Biomed. Opt. **18**, 050902 (2013).

3. Y. Zhang, B. Chen, and D. Li, "Propagation of polarized light in the biological tissue: a numerical study by polarized geometric Monte Carlo method," Appl. Opt. **55**, 2681–2691 (2016).

4. B. C. Wilson and G. Adam, "A Monte Carlo model for the absorption and flux distributions of light in tissue," Med. Phys. **10**, 824–830 (1983).

5. Q. Liu, C. Zhu, and N. Ramanujam, "Experimental validation of Monte Carlo modeling of fluorescence in tissues in the UV-visible spectrum," J. Biomed. Opt. **8**, 223–236 (2003).

6. Y. Hasegawa, Y. Yamada, M. Tamura, *et al.*, "Monte Carlo simulation of light transmission through living tissues," Appl. Opt. **30**, 4515–4520 (1991).

7. Q. Liu and N. Ramanujam, "Scaling method for fast Monte Carlo simulation of diffuse reflectance spectra from multilayered turbid media," J. Opt. Soc. Am. A **24**, 1011–1025 (2007).

8. P. Naglič, F. Pernuš, B. Likar, *et al.*, "Limitations of the commonly used simplified laterally uniform optical fiber probe-tissue interface in Monte Carlo simulations of diffuse reflectance," Biomed. Opt. Express **6**, 3973–3988 (2015).

9. C. Zhu, Q. Liu, and N. Ramanujam, "Effect of fiber optic probe geometry on depth-resolved fluorescence measurements from epithelial tissues: a Monte Carlo simulation," J. Biomed. Opt. **8**, 237–247 (2003).

10. T. Papaioannou, N. W. Preyer, Q. Fang, *et al.*, "Effects of fiber-optic probe design and probe-to-target distance on diffuse reflectance measurements of turbid media: an experimental and computational study at 337 nm," Appl. Opt. **43**, 2846–2860 (2004).

11. M. C. Skala, G. M. Palmer, C. Zhu, *et al.*, "Investigation of fiber-optic probe designs for optical spectroscopic diagnosis of epithelial pre-cancers," Lasers Surg. Med. **34**, 25–38 (2004).

12. B. Yu, A. Shah, V. K. Nagarajan, *et al.*, "Diffuse reflectance spectroscopy of epithelial tissue with a smart fiber-optic probe," Biomed. Opt. Express **5**, 675–689 (2014).

13. T. J. Pfefer, K. T. Schomacker, M. N. Ediger, *et al.*, "Multiple-fiber probe design for fluorescence spectroscopy in tissue," Appl. Opt. **41**, 4712–4721 (2002).

14. R. A. Schwarz, D. Arifler, S. K. Chang, *et al.*, "Ball lens coupled fiber-optic probe for depth-resolved spectroscopy of epithelial tissue," Opt. Lett. **30**, 1159–1161 (2005).

15. Q. Liu and N. Ramanujam, "Experimental proof of the feasibility of using an angled fiber-optic probe for depth-sensitive fluorescence spectroscopy of turbid media," Opt. Lett. **29**, 2034–2036 (2004).

16. N. Ramanujam, M. F. Mitchell, A. Mahadevan, *et al.*, "In vivo diagnosis of cervical intraepithelial neoplasia using 337-nm-excited laser-induced fluorescence," Proc. Natl. Acad. Sci. **91**, 10193–10197 (1994).

17. K.-B. Sung and H.-H. Chen, "Enhancing the sensitivity to scattering coefficient of the epithelium in a two-layered tissue model by oblique optical fibers: Monte Carlo study," J. Biomed. Opt. **17**, 107003 (2012).

18. T.-Y. Tseng, C.-Y. Chen, Y.-S. Li, *et al.*, "Quantification of the optical properties of two-layered turbid media by simultaneously analyzing the spectral and spatial information of steady-state diffuse reflectance spectroscopy," Biomed. Opt. Express **2**, 901–914 (2011).

19. Q. Liu and N. Ramanujam, "Sequential estimation of optical properties of a two-layered epithelial tissue model from depth-resolved ultraviolet-visible diffuse reflectance spectra," Appl. Opt. **45**, 4776–4790 (2006).

20. D. Arifler, R. A. Schwarz, S. K. Chang, *et al.*, "Reflectance spectroscopy for diagnosis of epithelial precancer: model-based analysis of fiber-optic probe designs to resolve spectral information from epithelium and stroma," Appl. Opt. **44**, 4291–4305 (2005).

21. Q. Wang, K. Shastri, and T. J. Pfefer, "Experimental and theoretical evaluation of a fiber-optic approach for optical property measurement in layered epithelial tissue," Appl. Opt. **49**, 5309–5320 (2010).

22. P. Singh, P. Pandey, S. Shukla, *et al.*, "Modelling, design and validation of spatially resolved reflectance based fiber optic probe for epithelial precancer diagnostics," Appl. Sci. **10**, 8836 (2020).

23. A. M. Wang, J. E. Bender, J. Pfefer, *et al.*, "Depth-sensitive reflectance measurements using obliquely oriented fiber probes," J. Biomed. Opt. **10**, 044017 (2005).

24. N. Nemichand, S. Shukla, P. Singh, *et al.*, "Optimization of source-detector separation for enhanced spatially resolved fluorescence from epithelial layer," Proc. SPIE **13010**, 130100 (2024).

25. Nemichand, S. Shukla, B. S. Deo, *et al.*, "Smartphone-based bimodal device (SBBD) for oral precancer diagnosis and biopsy guidance in clinical settings," Opt. Lett. **50**, 1993–1996 (2025).

26. S. Shukla, C. Vishwakarma, A. N. Sah, *et al.*, "Smartphone-based fluorescence spectroscopic device for cervical precancer diagnosis: a random forest classification of *in vitro* data," Appl. Opt. **62**, 6826–6834 (2023).

27. I. Georgakoudi, B. C. Jacobson, M. G. Muller, *et al.*, "NAD(P)H and collagen as *in vivo* quantitative fluorescent biomarkers of epithelial precancerous changes," Cancer Res. **62**, 682–687 (2002).

28. Y. Pu, W. Wang, G. Tang, *et al.*, "Changes of collagen and nicotinamide adenine dinucleotide in human cancerous and normal prostate tissues studied using native fluorescence spectroscopy with selective excitation wavelength," J. Biomed. Opt. **15**, 047008 (2010).

29. Y. Jing, Y. Wang, X. Wang, *et al.*, "Label-free imaging and spectroscopy for early detection of cervical cancer," J. Biophotonics **11**, e201700245 (2018).

30. B. L. Meena, A. Agarwal, C. Pantola, *et al.*, "Concentration of FAD as a marker for cervical precancer detection," J. Biomed. Opt. **24**, 1–7 (2019).

31. A. K. Barik, S. Pavithran, M. V. Pai, *et al.*, "Laser induced fluorescence of cervical tissues: an in-vitro study for the diagnosis of cervical cancer from the cervicitis," J. Opt. **24**, 054002 (2022).

32. P. Kumar, S. K. Kanaujia, A. Singh, *et al.*, "In vivo detection of oral precancer using a fluorescence-based, in-house-fabricated device: a Mahalanobis distance-based classification," Lasers Med. Sci. **34**, 1243–1251 (2019).

33. S. K. Chang, D. Arifler, R. Drezek, *et al.*, "Analytical model to describe fluorescence spectra of normal and preneoplastic epithelial tissue: comparison with Monte Carlo simulations and clinical measurements," J. Biomed. Opt. **9**, 511–522 (2004).

34. G. Bhowmick, N. Gautam, and L. Gantayet, "Design optimization of fiber optic probes for remote fluorescence spectroscopy," Opt. Commun. **282**, 2676–2684 (2009).

35. H. Shhadeh, W. Bachir, and G. Karraz, "A sensitive fibre optic probe for autofluorescence spectroscopy of oral tongue cancer: Monte Carlo simulation study," Biomed. Res. Int. **2020**, 1936570 (2020).

36. A. Shatskaya, D. Artemyev, and I. Bratchenko, "Modeling of fiber optic probes for selective fluorescence sensing of multilayered biological tissues," J. Appl. Spectrosc. **87**, 112–120 (2020).

37. T. J. Pfefer, A. Agrawal, and R. A. Drezek, "Oblique-incidence illumination and collection for depth-selective fluorescence spectroscopy," J. Biomed. Opt. **10**, 044016 (2005).

38. F. Jaillon, W. Zheng, and Z. Huang, "Beveled fiber-optic probe couples a ball lens for improving depth-resolved fluorescence measurements of layered tissue: Monte Carlo simulations," Phys. Med. Biol. **53**, 937 (2008).

39. M. S. Nair, N. Ghosh, N. S. Raju, *et al.*, "Determination of optical parameters of human breast tissue from spatially resolved fluorescence: a diffusion theory model," Appl. Opt. **41**, 4024–4035 (2002).

40. D. E. Hyde, T. J. Farrell, M. S. Patterson, *et al.*, "A diffusion theory model of spatially resolved fluorescence from depth-dependent fluorophore concentrations," Phys. Med. Biol. **46**, 369 (2001).

41. G. Ma, J.-F. Delorme, P. Gallant, *et al.*, "Comparison of simplified Monte Carlo simulation and diffusion approximation for the fluorescence signal from phantoms with typical mouse tissue optical properties," Appl. Opt. **46**, 1686–1692 (2007).

42. S. Gupta, V. S. Raja, and A. Pradhan, "Simultaneous extraction of optical transport parameters and intrinsic fluorescence of tissue mimicking model media using a spatially resolved fluorescence technique," Appl. Opt. **45**, 7529–7537 (2006).

43. J. Swartling, A. Pifferi, A. M. Enejder, *et al.*, "Accelerated Monte Carlo models to simulate fluorescence spectra from layered tissues," J. Opt. Soc. Am. A **20**, 714–727 (2003).

44. S. Shukla, B. S. Deo, Nemichand, *et al.*, "Spatially resolved fibre-optic probe for cervical precancer detection using fluorescence spectroscopy and PCA-ANN-based classification algorithm: an in vitro study," J. Biophotonics **17**, e202400284 (2024).

45. Q. Wang, H. Yang, A. Agrawal, *et al.*, "Measurement of internal tissue optical properties at ultraviolet and visible wavelengths: development and implementation of a fiberoptic-based system," Opt. Express **16**, 8685–8703 (2008).

46. I. Pavlova, C. R. Weber, R. A. Schwarz, *et al.*, "Fluorescence spectroscopy of oral tissue: Monte Carlo modeling with site-specific tissue properties," J. Biomed. Opt. **14**, 014009 (2009).

47. Y. H. Ong, J. C. Finlay, and T. C. Zhu, "Monte Carlo modelling of fluorescence in semi-infinite turbid media," Proc. SPIE **10492**, 104920T (2018).

48. M. S. Patterson and B. W. Pogue, "Mathematical model for time-resolved and frequency-domain fluorescence spectroscopy in biological tissues," Appl. Opt. **33**, 1963–1974 (1994).

49. D. Arifler, C. MacAulay, M. Follen, *et al.*, "Spatially resolved reflectance spectroscopy for diagnosis of cervical precancer: Monte Carlo modeling and comparison to clinical measurements," J. Biomed. Opt. **11**, 064027 (2006).

50. M. Kamal, "Cervical pre-cancers: biopsy and immunohistochemistry," Cytojournal **19**, 38 (2022).

51. T. J. Pfefer, L. Matchette, and R. Drezek, "Influence of illumination-collection geometry on fluorescence spectroscopy in multilayer tissue," Med. Biol. Eng. Comput. **42**, 669–673 (2004).

52. M.-A. Mycek and B. W. Pogue, *Handbook of Biomedical Fluorescence* (CRC Press, 2003).

53. U. Utzinger and R. R. Richards-Kortum, "Fiber optic probes for biomedical optical spectroscopy," J. Biomed. Opt. **8**, 121–147 (2003).

54. I. Damjanov, "The female genital tract and breasts," in *Pathology Secrets*, 3rd ed., I. Damjanov, ed. (Mosby, 2009), pp. 339–364, chap. 17.

55. M. Muntean, C. Simionescu, R. Taslîcă, *et al.*, "Cytological and histopathological aspects concerning preinvasive squamous cervical lesions," Curr. Health Sci. J. **36**, 26–32 (2010).